Joule

CellPress

Article

Electrical edge effect induced photocurrent overestimation in low-light organic photovoltaics

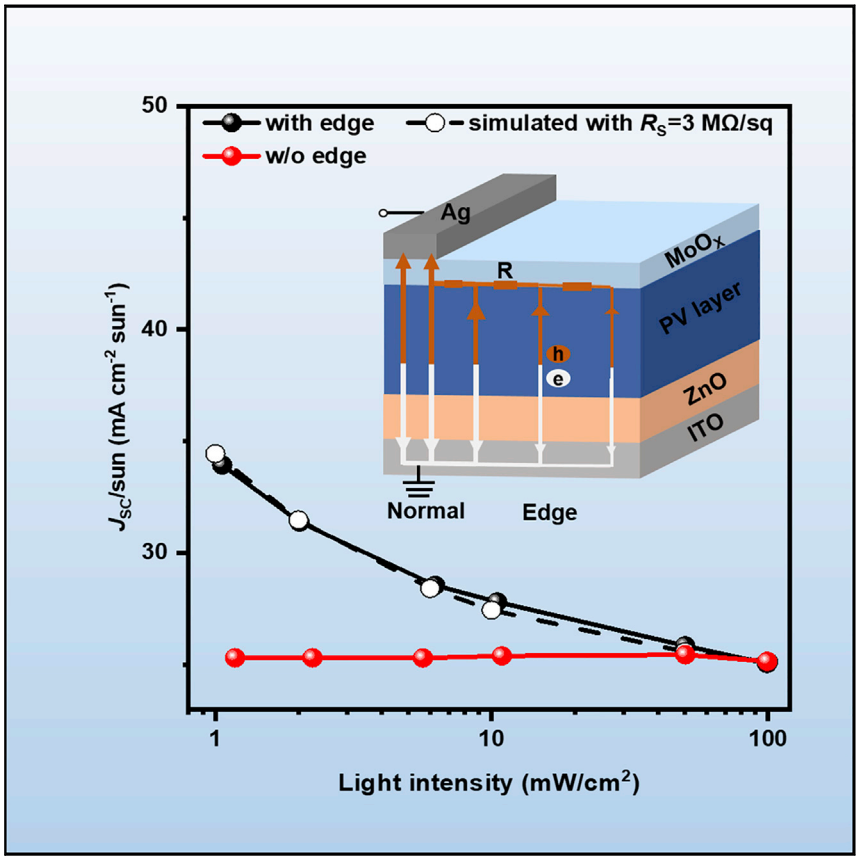

The short-circuit current (J_{SC}) overestimation is a severe but common issue in low-light photovoltaic devices. This work demonstrated that the electrical edge effect, whether originated from conducting layer or interface doping, will lead to significant J_{SC} and power-conversion efficiency overestimation of more than 100%. Furthermore, this work showed that large surface roughness leads to a stronger electrical edge effect through reduced smaller sheet resistance.

Xiaobo Zhou, Chao Zhao, Awwad Nasser Alotaibi, ..., Zaifei Ma, Brian A. Collins, Wei Ma

zhaochao@xjtu.edu.cn (C.Z.)
brian.collins@wsu.edu (B.A.C.)
msewma@xjtu.edu.cn (W.M.)

Highlights

J_{SC} overestimation is a severe but common issue in low-light photovoltaic devices

At low light, electrical edge effect could lead to a J_{SC} overestimation of more than 100%

Interface doping would result in a strong electrical edge effect

Large surface roughness leads to a stronger electrical edge effect through reduced R_S

Zhou et al., Joule 6, 1904–1917
August 17, 2022
https://doi.org/10.1016/j.joule.2022.06.008

CellPress

Joule

Article

Electrical edge effect induced photocurrent overestimation in low-light organic photovoltaics

Xiaobo Zhou,[1] Chao Zhao,[1,*] Awwad Nasser Alotaibi,[2] Hongbo Wu,[3] Hafiz Bilal Naveed,[1] Baojun Lin,[1] Ke Zhou,[1] Zaifei Ma,[3] Brian A. Collins,[2,*] and Wei Ma[1,4,*]

SUMMARY

In many literatures, the short-circuit current (J_{SC}) of indoor organic photovoltaics is overestimated, leading to severely wrong device performance evaluation and analysis. In this work, based on the equivalent circuit model, we demonstrate that electrical edge effect is sensitive to both transverse surface resistance and light intensity. At low light intensity, the electrical edge effect could lead to J_{SC} being significantly overestimated, i.e., by 100% and even more. We show that for a PM6:Y6 device capped with a MoO_X layer, when measured under 0.01 sun, the usually overlooked interface doping mechanism would lead to J_{SC} and PCE overestimation by 51% and 15%, respectively. Besides, we show that the magnitude of J_{SC} overestimation drastically increases with high photoactive-layer surface roughness. This work emphasized the significant electrical edge effect on J_{SC} evaluations for low-light solar cells and is conducive to understanding the intrinsic mechanism of edge effect, promoting a healthier development of organic photovoltaics.

INTRODUCTION

Attributed to the expeditious progress of non-fullerene acceptors, the power-conversion efficiencies (PCEs) of the bulk heterojunction organic photovoltaics (OPVs) have exceeded 18% for single-junction cells under AM 1.5G (1 sun light intensity).[1–5] In recent years, benefiting from its unique performance advantages, indoor OPVs have attracted significant research interest with PCE over 28%.[5–7] However, although any further PCE improvement is very encouraging, it has been demonstrated that sometimes, the short-circuit current (J_{SC}) could be overestimated by 10%.[8–10] Such J_{SC} overestimation issue is more severe for low-light-intensity devices. Figure 1A summarized J_{SC} overestimation factor (defined here as $\frac{J_{sc}\ (sun)}{J_{sc}(1\ sun)\ \times\ (sun\ number)}$, where J_{SC} (sun) is short-circuit current under certain sun light intensity and sun number is the light intensity in sun units) that measured under different light intensity from literatures, where J_{SC}/sun under 0.01 sun could be 80% higher than that under 1 sun (Figure S1), leading to overestimated PCE.[10–14] Some perovskite solar cells and dye-sensitized solar cells (DSSCs) have also reported abnormally high J_{SC}/sun and thus PCE at low light intensity.[15–17] Such high J_{SC}/sun indicates an external quantum efficiency (EQE) of much higher than 100%, which is impossible for those device systems. Consequently, the device performance evaluation and corresponding analysis such as optical changes or carrier dynamic mechanisms are compromised. Furthermore, J_{SC} versus light intensity plot has been commonly used to analyze the bimolecular recombination. However, J_{SC} overestimation under low light intensity would result in artificially overestimated bimolecular recombination coefficient α, thus misleads the corresponding analysis of device

CONTEXT & SCALE

In many literatures, the short-circuit current (J_{SC}) of indoor organic photovoltaics is overestimated, leading to a severely wrong evaluation and analysis of device performance. Based on equivalent circuit model, we demonstrate that electrical edge effect is sensitive to both interface layer resistance and light intensity. At low light intensity, electrical edge effect could lead to J_{SC} being more significantly overestimated, i.e., by 100% and more. We showed that for a PM6:Y6 device capped with a MoO_X layer, when measured under 0.01 sun, the usually overlooked interface doping mechanism would lead to J_{SC} and PCE overestimation by as much as 51% and 15%, respectively. Besides, we demonstrate that the magnitude of J_{SC} overestimation drastically increases with high photoactive-layer surface roughness. This work emphasized the significant edge effect on J_{SC} evaluations for low-light solar cells and is conducive to understanding the intrinsic mechanism of edge effect, promoting their healthier development.

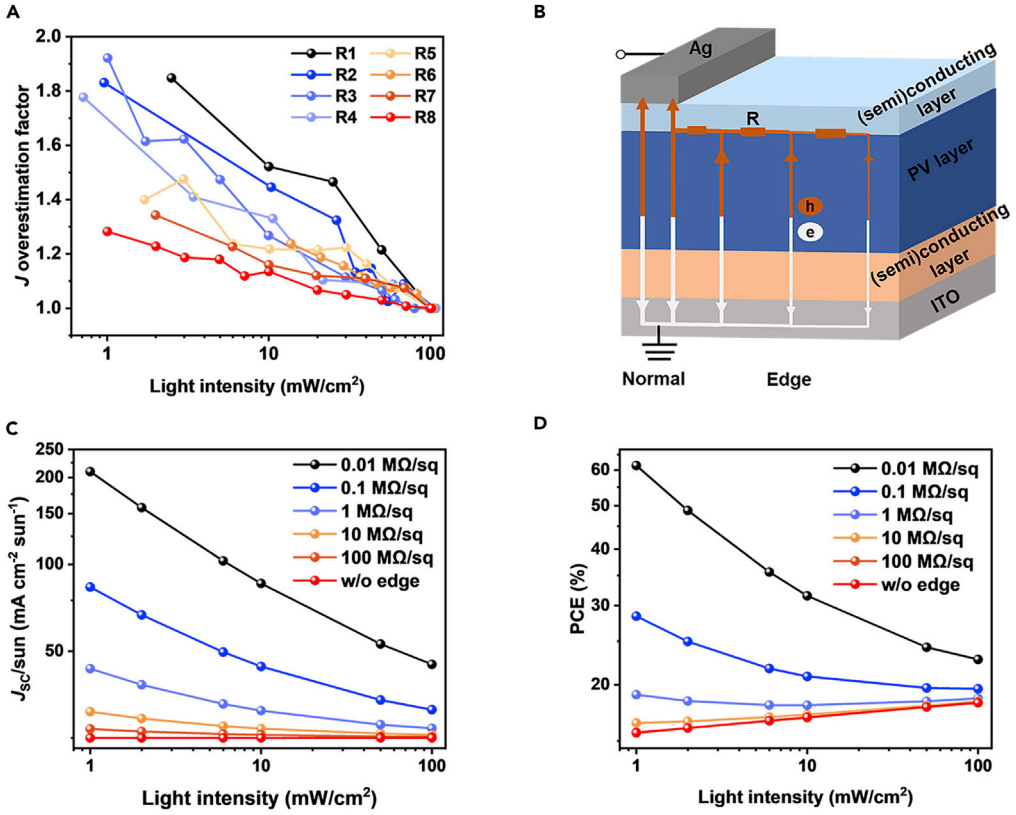

Figure 1. The J_{SC} overestimation of various material systems under different light intensities and device structures

(A) The J_{SC} overestimation factor of the reference papers (R1–R8) under different light intensities.[18–25]

(B) Schematic diagram of the simplified circuit model of the electrical edge effect. The current line width represents relative current density at different distance from edge.

(C) Simulated J_{SC}/sun under different light intensities with varied transverse surface R_S.

(D) Simulated PCE based on varied transverse surface resistance of active layer under different light intensities.

recombination dynamics and the development of optimization strategies. Therefore, much deliberation is required in terms of the accurate measurement of J_{SC}.

The overestimation of J_{SC} is usually attributed to area misestimate, optical factor, and electrical factors.[8,13,26,27] The optical factors includes spectral mismatch and stray light effects. The spectral difference between the light sources employed and AM 1.5G accounts for the spectral mismatch, which has usually been taken care of by pre-calibrating the input optical source (AM1.5G) and reference cell spectral response.[28,29] The stray light includes non-vertical, non-parallel, and/or scattering light.[12,26–28,30] Mask and properly calibrated light source are often recommended to determine the effective photovoltaic area and current density.[26,28] However, applying mask will inevitably reduce the open-circuit voltage (V_{OC}) because the photocurrent would be counterbalanced by the injection current in the masked area.[31] Besides, the fill factor (FF) may also be overestimated due to the varied series resistance.[31,32] These will cause a comprehensive influence on the evaluation of PCE. Without mask, both optical and electrical-factor-induced edge effect becomes the main contribution for J_{SC} overestimation.[33] For common device (4 mm^2), the optical-factor-induced edge effect leads to an J_{SC} overestimation of no more than 10%.[13] By contrast, the electrical-factor-induced edge effect, where interface (semi)conducting layers act as horizontal charge transport channel so that the photocurrent generated out of main device

[1]State Key Laboratory for Mechanical Behavior of Materials, Xi'An Jiaotong University, Xi'an 710049, China

[2]Department of Physics and Astronomy, Washington State University, Pullman, WA 99164, USA

[3]Center for Advanced Low-Dimension Materials, State Key Laboratory for Modification of Chemical Fibers and Polymer Materials, College of Materials Science and Engineering, Donghua University, Shanghai 201620, China

[4]Lead contact

*Correspondence: zhaochao@xjtu.edu.cn (C.Z.), brian.collins@wsu.edu (B.A.C.), msewm@xjtu.edu.cn (W.M.)

https://doi.org/10.1016/j.joule.2022.06.008

area gets collected, could contribute to J_{SC} more. Extensive works have focused on the electrical edge effect; for example, one of the classic models proposed by Brabec et al.[9] shows that in indium tin oxide (ITO)/PEDOT:PSS/PV layer/Al device architecture, the highly conductive PEDOT:PSS can transversely transfer the holes generated at the edge area to the electrode, leading to assignable edge effect.[12] Under standard 1 sun illumination, even with a resistivity of 10^{-1} Ω cm (which is 100 times higher compared with the commercial PH1000 recipe), photocurrent would be effectively collected at 300 μm away from the edge, which leads to an overall overestimation of J_{SC} of about 43%. Similar charge-collection-layer-induced edge effect is observed in ZnO systems.[33]

Although electrical edge effect has been studied in some previous literatures, the significant effect of light intensity on electrical edge effect has never been appreciated. In fact, the key physics parameter that determines electrical edge contribution is the voltage distribution instead of the resistance. Therefore, in addition to the resistance, electrical edge effect could also be strongly affected by photocurrent (either light intensity or photoactive layer system). Even for the same interlayer resistance, lower photocurrent leads to lower voltage drops at certain distance outside edge and thus stronger J_{SC} overestimation. For low photocurrent conditions such as indoor OPVs, the edge effect would be much more significant since the photocurrent is usually 2–3 orders of magnitude lower than the normal sunlight conditions. For the same reason, indoor OPVs electrical edge effect would be significant even if the interlayer conductivity is low such that the edge effect is negligible for 1 sun conditions. Such a concept is theoretically straightforward but has never been evaluated for indoor OPVs systems.

In this work, the equivalent circuit model is utilized to quantitatively investigate the effect of light intensity and transverse sheet resistance (R_S) on J_{SC} overestimation. Simulation showed that under 0.01 sun light intensity, with 1 MΩ/sq R_S, the electrical edge effect will lead to significantly overestimated J_{SC} and PCE by over 70% and 22%, respectively. Since the electrical edge effect in our model is irrelevant to the light source or photoactive layer (PAL) absorption spectral, the simulation conclusions apply to all types of solar cells, including perovskite solar cell and DSSCs. We then demonstrate that the usually overlooked interface doping mechanism (MoO_X-induced doping on surface of active layer) could lead to significant edge effect: under 0.01 sun, the PM6:Y6 (1% 1-chloronaphthalene [CN]) device J_{SC}, and thus, PCE could be overestimated by 51% and 15%, respectively. Normalized absorption spectrum, PL measurements, EQE measurements, and current mapping measurements were utilized to rule out the other possible mechanism and confirmed the electrical edge effect. Besides, we analyzed the relationship among surface morphology of active layer and surface resistance and the consequent electrical edge effect, where the magnitude of J_{SC} overestimation increases significantly with surface roughness. Our work confirms that the electrical edge effect would induce severe errors in the low-light-device measurement and analysis, also in bimolecular recombination analysis. The intrinsic mechanism of the influence of electrical edge effect on the J_{SC} and efficiency is better revealed, which provide guidance for more accurate measurements of current and efficiency in OPV fields.

RESULTS AND DISCUSSION

Computational study of light intensity and transverse-resistance-dependent edge effects

In order to quantify the variation of transverse resistance and light intensity on edge photocurrent contribution, we adopted the classic equivalent circuit model but

added series resistance at the edge area contributions, as shown in Figures 1B and S2. The "measured" photocurrent is the summation of main device area (sandwiched with electrodes) with adjacent edge areas (lack of top metal electrode). We applied the commonly used small device area, 4 mm^2, in our model to evaluate the edge effects. The edge-area photocurrent at two sides (ITO strip) passes through an effective resistor before getting collected by the corresponding electrode. Therefore, the electric condition of edge area slice n satisfies the following equations:

$$V_n = V_o - \int_o^n R_n J_n dl$$

$$J_n = J_{Ph} - J_0\left(e^{\frac{V_n}{kT}} - 1\right),$$

where R_n is the sheet resistance at each slice n and J_n is the corresponding photocurrent. The details of our model are described in the Note S1 in supplemental information. As shown in Figure S3A, in the scenario consisting of an efficient device delivering a photocurrent of 25 mA cm^{-2} and containing a (semi)conducting film with sheet resistance of 1 MΩ/sq, edge photocurrent at only 70 μm away (which is much smaller than device size) could be effectively collected. However, as light intensity and (thus) photocurrent intensity decrease, photocurrent generated at farer distance would be effectively collected. The obvious turning point of each slice's photocurrent also extends to a farther distance as the edge resistance decreases. Figure 1C summarized the simulated J_{SC}/sun with varied light intensity and R_S, in the range from 0.01 to 100 MΩ/sq, which is the typical resistance of commercial Al4083 poly(3,4-eth-ylene-dioxythiophene):(styrene sulfonate) (PEDOT:PSSH) films. As shown in Figure S3B, the J_{SC} drastically increases at low surface R_S and under low light. At certain light intensity, the edge photocurrent contribution decreases as voltage increases (J_{SC} at any voltage is still overestimated); similarly, at a certain voltage, as light intensity decreases, the edge photocurrent contribution increases (shown in Figures S3C and S3D). As a result, FF decreases with stronger electrical edge effect (Figure S3E). On the other hand, since the edge area photocurrent is always in the same direction as in main area, V_{OC} does not change with the electrical edge effect (shown in Figure S2 and Table S1). Therefore, despite FF decrement, J_{SC} and thus PCE still significantly increase with the electrical edge effect. For example, for 1 MΩ/sq, the edge photocurrent contribution is 7% at 1 sun illumination, which drastically increases to over 70% as light illumination intensity decreases to 0.01 sun, leading to PCE overestimation of 22%. For the case of 0.1 MΩ/sq R_S, electrical edge contribution at 0.01 sun will increase to 230%, leading to J_{SC} and PCE overestimation of almost 2.3 and 0.8 times, respectively. Such severe J_{SC} and PCE overestimation would outperform any real device optimization endeavors. Therefore, special care must be taken for the edge effect of indoor device measurements. It should be noted that even though the electrical edge effect decreases with device size, at low light, even for 2 × 2 cm device, this could still cause a 20% J_{SC} overestimation (shown in Figure S5).

Experimental validation of the electrical-edge-effect-induced J_{SC} overestimation

The resistance evaluation in edge effect is usually only focusing on the transport layers (charge collection layer) because the conductivity of intrinsic or even photoexcited photoactive layer is much lower than the transport layer, and thus, it has negligible effect. To demonstrate the electrical edge effect, we first fabricated a device with the structure of ITO/ZnO/PM6:Y6/PEDOT:PSSH/Al, where PEDOT:PSSH is a typical conducting layer with R_S of 6.7 MΩ/sq. As shown in Figure S6, the J_{SC}/sun increases as light intensity decreases, and the simulation with R_S = 6.7 MΩ/sq fits the

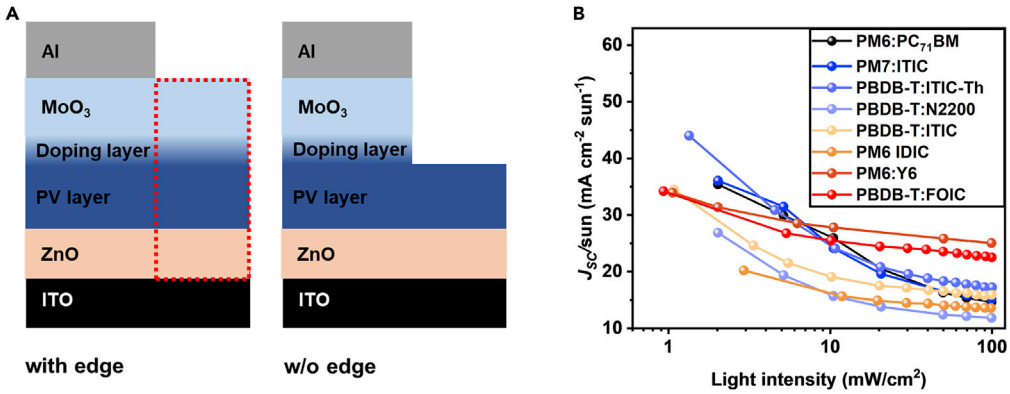

Figure 2. The J_{SC} overestimation of various material systems under different light intensities and device structures

(A) Device structures with and without edge.

(B) Dependence of the J_{SC}/sun on light intensity of various photoactive layer systems involved in our work.

experimental results very well in the whole light intensity range. Using charge collecting layers with higher conductivity will lead to more severe J_{SC} overestimation. However, interface-doping-induced conductivity has been overlooked. The highly doped charge extraction layers with deep (>5.2 eV) or shallow (<4 eV) work function (WF) is commonly used to achieve ohmic contact and soft-fermi pinning to reduce contact resistance, enhance built-in potential and effective mobility, and thus FF and V_{OC}.[34,35] As a result of the ohmic contact, delta charge transfer with a doping level of 10^{11} cm^{-2} due to interface charge transfer has been measured at PEDOT:PSSH/PAL interface.[36] MoO_X is the commonly used hole collection layer due to its deep WF (~6.9 eV), leading to much higher interface carrier density than that of the PEDOT:PSSH/PAL interface. Considering carrier mobility of ~10^{-3} cm^2 V^{-1} s^{-1} and an effective doping depth of ~10 nm, this gives an interface layer R_S in the order of 1–100 MΩ/sq, which is comparable with the commercial Al4083 PEDOT:PSSH.[37] Therefore, even for device with no apparent conducting film, such interface doped layer is sufficient for significant edge effect under low illuminations. To the best of our knowledge, such interface-doping-induced electrical edge effect has never been considered in the literatures. Similar interface doping effects will occur when electron collection layers with WF shallower than 4.0 eV is applied.[38]

To experimentally validate such interface-doping-induced electrical edge effect, we fabricated devices with and without MoO_X-capped edge, as shown in Figure 2A. Since the only difference between the two structures is the MoO_X-capped edge, considering that MoO_X is practically insulating,[37] any device performance difference would be attributed to the MoO_X/PAL layer interfaces at edge. J_{SC} was collected under the light intensity from 1 (0.01 sun) to 100 mW/cm^2 (1 sun). We also tested different photoactive material systems, including PBDBT:ITIC, PM6:IDIC, PM6:Y6, etc., with the same device structure to confirm the generality of the phenomenon. As shown in Figure 2B, for the MoO_X devices with edges, as light intensity decreases from 1 to 0.01 sun, J_{SC}/sun all significantly increase, regardless of the photoactive layer systems (the *J-V* curves are shown in Figure S7). Same trend was observed when measured with increased light intensity (Figure S8A) to exclude any hysteresis effects. As shown in Figure S8B, the highest J_{SC} overestimation factor is increased to more than 2.5 at 0.01 sun, this means the "measured" J_{SC} is overestimated by more than 150%. By contrast, without MoO_X-capped edge, the J_{SC} overestimation factor only improve by <2% as light intensity decreases to 0.01 sun, which could be mainly attributed to the reduced recombination losses.

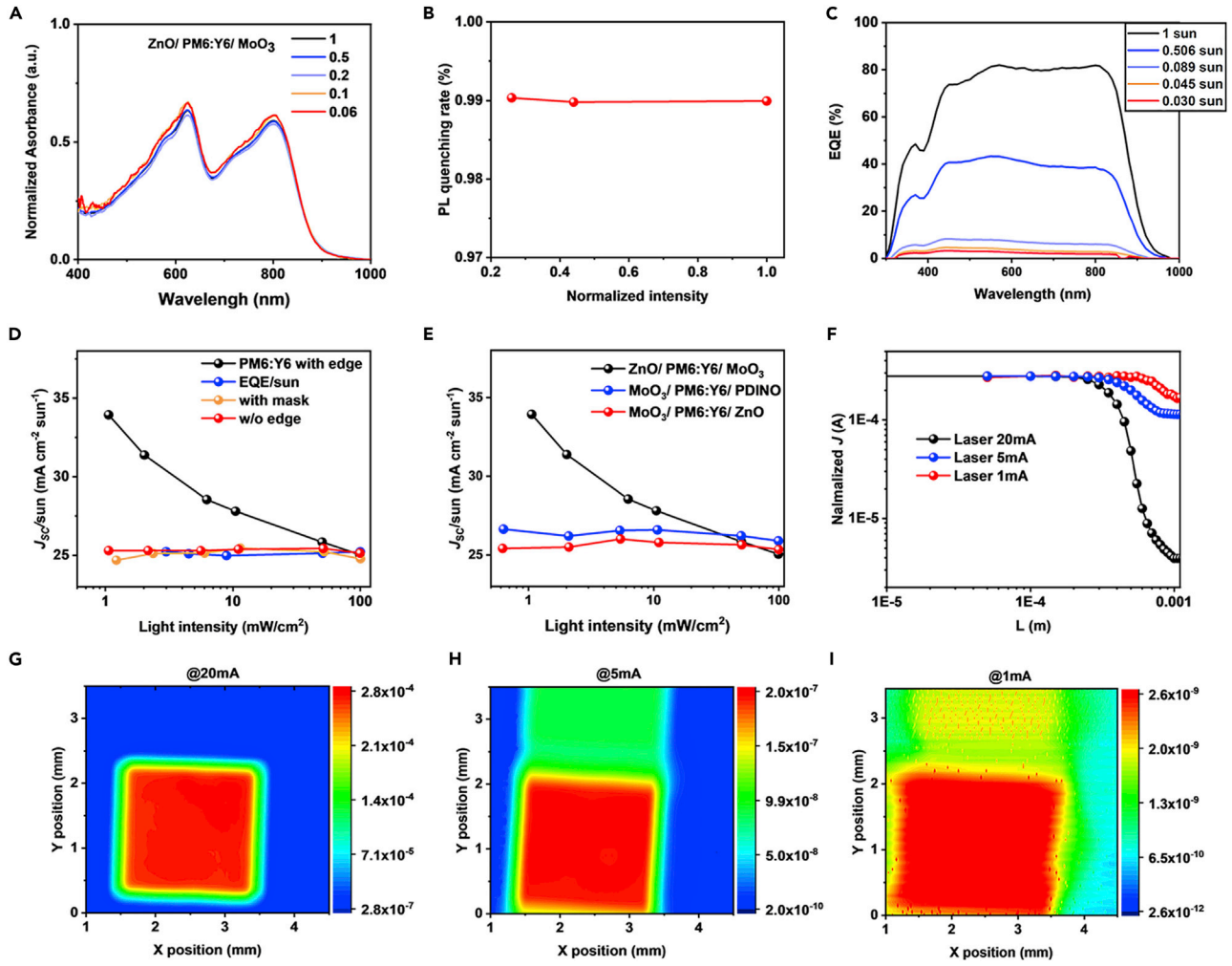

Figure 3. Dependence of MoO_X-induced electrical edge effect on light intensity

(A) Normalized absorption spectrum by light intensity of ZnO/PM6:Y6/MoO_X device.

(B) Dependence of PL quenching rate on light intensity. The largest light intensity used in absorption and PL is normalized to 1.

(C) EQE spectra under various light intensities.

(D) Dependence of J_{SC}/sun on light intensity for the inverted devices of PM6:Y6 with edge, with mask and without edge, and dependence of EQE/sun on light intensity.

(E) Dependence of J_{SC}/sun on light intensity for the devices with various interlayers.

(F–I) (F) Normalized edge distance dependent current under different excitation currents acquired from photocurrent mapping test; corresponding photocurrent mapping of devices using a laser with excitation currents of (G) 20, (H) 5, and (I) 1 mA.

Ruling out other artifacts

We applied PM6:Y6 OPV system to further exclude the absence of any confounding variations in the absorption and charge generation properties at different illuminations.

The UV-vis absorption spectrum of ZnO/PM6:Y6/MoO_X was collected under different light intensities. The absorbance spectrum normalized by light intensity (Figure 3A) does not emerge any prominent change with variation of light intensity from 1 to 0.06 sun, which eliminates the possibility of absorption changes on J_{SC}/sun under various light intensities. Photoluminescence (PL) analysis shows the similar exciton dissociation behavior under different light intensities; therefore, the J_{SC} increment is not due to exciton dissociation (Figures 3B and S9; Table S2).[39,40]

The light-dependent EQEs, however, indicate that the J_{SC}/sun parameter remains unchanged in the whole light intensity range (Figures 3C and 3D), which is primarily because the light spot of EQE setup is smaller than device area. This brings out the idea that for EQE measurement, one shall make sure the light spot size is smaller than device area in order to avoid any edge-effect artifacts. When mask is applied to exclude the edge part, the J_{SC}/sun also remains nearly unchanged with decreased light intensity, same as the EQE results and the device without edge results (Figure 3D). Besides, we have shown that stray light only has very limited effects (<5%) on the J_{SC} overestimation where J_{SC}/sun measured with tilted light remains constant in the whole light intensity range (Figure S10). Therefore, MoO_X-induced electrical edge effect is the main cause of J_{SC} overestimation under low light intensities.

To confirm the WF effect, we fabricated conventional devices with thermally evaporated MoO_X. Photoactive layer, i.e., PM6:Y6, is then spin coated onto the MoO_X film, followed by 3,3′-(1,3,8,10-tetraoxoanthra[2,1,9-def:6,5,10-d′e′f′]diisoquinoline-2,9(1H,3H,8H,10H)-diyl)bis(N,N-dimethylpropan-1-amine oxide) (PDINO) or ZnO film castings and metal electrode evaporations. Since MoO_X is highly susceptible to absorb water and oxygen in the solution, despite its high WF under vacuum condition, once exposed to glovebox environment and/or solvent treatment, the WF will reduce to around 5.4 eV, leading to much lower interface hole doping.[41,42] As expected, the conventional devices, either capped with PDINO or ZnO, do not show any edge effect under low light intensity, as shown in Figures 3E, S11, and S12. Therefore, it can be concluded that the low interface resistance induced by high WF is the key origin for electrical edge effect.

The current mapping test employing a focused laser scanning over the device is utilized to further confirm the contribution of edge currents during *J-V* measurement.[12,33] The light intensity of laser is controlled by the input current, and the light intensity of laser increases as the input current increases. As shown in Figures 3G–3I, the current mapping test confirmed the additional current generated in the edge area. Figure 3F shows the relationship between edge current and edge distance. As light intensity decreases, the normalized edge current extends further; thus, the additional current generated in the edge part has a greater impact on the effective current, which is consistent with equivalent circuit model simulations. The current mapping test provides direct evidence on the light-intensity-dependent electrical edge effect.

To check for the self-consistency with the effect of edge conductivity and light intensity on J_{SC} overestimation, we computed the J_{SC}/sun of PM6:Y6 system using reasonable interface conductivity. We first considered a simple model to estimate the resistance of interface doping layer. Taking MoO_X/PM6 interface doping intensity N as $\sim 10^{21}$ cm^{-3} with an effective doping depth d of 10 nm and bulk hole mobility of $\sim 10^{-3}$ $cm^{-2}\,V^{-1}\,s^{-1}$ (as shown in Figure S13 and Table S3), we could get an effective conducting channel with $R_S \sim 6$ MΩ/sq ($1/eN\mu d$), where μ is the hole-density-dependent mobility following the Figure 1 in Zhou et al.[36] The simulated J_{SC}/sun vs sun intensity trend matches the experimental results fairly well (Figure S14A), without any tuning parameter needed. The simulation also fits the J_{SC}/sun trend of larger area device (16 mm^2) very well when using the same model and parameters.

The effect of morphology on J_{SC} overestimation

Despite J_{SC} overestimation increases with decreased sun intensity, we noted that the magnitude of J_{SC} overestimation varies with different systems, from 50% to more than 200% at 0.01 sun intensity (Figure S8B). The intrinsic properties, including light

Table 1. Photovoltaic parameters of the corresponding devices under 1 sun illumination

Condition	V_{OC} (V)	J_{SC} (mA cm^{-2})	FF (%)	PCE (%)	J_{EQE}[a] (mA cm^{-2})	Deviation[b] (%)
0% CN	0.835 ± 0.007	25.61 ± 0.27	66.06 ± 0.59	14.16 ± 0.20	24.41	4.92
1% CN	0.842 ± 0.005	25.74 ± 0.32	72.23 ± 0.67	15.66 ± 0.35	24.48	5.15
1.5% CN	0.852 ± 0.003	23.03 ± 0.34	65.36 ± 1.07	12.82 ± 0.48	21.03	9.62
2% CN	0.836 ± 0.002	16.68 ± 0.28	58.39 ± 1.16	8.16 ± 0.53	15.04	10.9

[a]J_{EQE} is calculated by EQE and the deviation is the rate of difference between current and EQE; the average parameters were calculated from more than 10 independent cells. The effective area of the device is 0.04 cm^2.
[b]Deviation is calculated by (J_{SC} -J_{EQE})/J_{EQE}.

absorption, recombination, and carrier mobility, are unlikely to give such significant J_{SC}/sun increment (calculated with different *J-V* curves, as shown in Figure S14B). Considering that these devices have similar interface layers and the MoO_X film is nearly insulating, such J_{SC}/sun variation may be related to morphology differences, especially at the interface. To understand this, the efficient system PM6:Y6 is adopted to further investigate the influence of morphology on such edge effect induced J_{SC} overestimation. CN was applied as additive to control the morphology. The device performances of various CN contents under 1 sun are summarized in Table 1, and the *J-V* curves under different light intensities are displayed in Figure S15. It is found that although J_{SC}/sun increases as light intensity decreases, its amplitude increases with the increase of CN contents (Figure 4A). The CN-controlled morphology is characterized through grazing incidence wide-angle X-ray scattering (GIWAXS),[43,44] as illustrated in Figures S16 and 4B. The variation of the coherence length (CL) of π-π stacking (Table S4) may account for the difference of their corresponding J_{SC} and also the EQE (Figure S17) under 1 sun intensity. Besides, as CN content increases, the (100) stacking CL keeps increasing, indicating enhanced crystallinity. The strong crystallinity facilitates the phase separation (the TEM shown in Figure S18), possibly leading to increased surface roughness (from 0.9 to 2.0 to 20.4 to 43.4 nm, as shown in Figure 4C).[45] The J_{SC} overestimation could be sensitive to surface roughness changes. To check this, we fabricated PM6:Y6 devices with the same structure but varied annealing temperature (the atomic force microscopy [AFM] shown in Figure S19) and PBDB-T:ITIC and PCE10:IEICO devices (Figures S20 and S21) with different 1,8-Diiodooctane (DIO) contents to modulate the surface roughness. As shown in Figure 4D, at 0.01 sun intensity, J_{SC}/sun shows clear increasing trend with increased surface roughness. We also simulated the J_{SC}/sun curves for the three systems, and the simulated J_{SC}/sun factor fitted the experimental results well by only changing surface R_S, as shown in Figures S14 and S22. To confirm that surface roughness affected the doping-induced surface R_S, we adopted the glass/PM6:Y6/MoO_X/Al device structure to measure the R_S of interface doping layer, as shown in Figure S23A. Since intrinsic PM6:Y6 and MoOx layers are nearly insulating, upon applied voltage, the current can only transversely transport through the interface doping layer. The surface R_S of PM6:Y6 film with 0% CN, 1% CN, and 1.5% CN is 2.53, 1.74, and 0.46 MΩ/sq, respectively. Therefore, the surface R_S indeed decreases with increased surface roughness. In addition, the simulated R_S matches with the pure film R_S well in the corresponding solar cells: for PM6:Y6 device with 0%, 1%, and 1.5% CN, the simulated R_S is 3, 1.5, and 0.5 MΩ/sq, respectively. This confirms that surface roughness leads to higher J_{SC} overestimation through decreased R_S. We suppose that this could be due to two reasons: (1) rough surface is usually a consequence of high crystallinity,[45] which leads to higher carrier mobility and thus lower R_S (by μ change) and (2) rough surface could lead to an effectively thicker carrier transport channel, which essentially decreases the R_S (*d* change), as illustrated in Figure S23B. In fact, although surface roughness

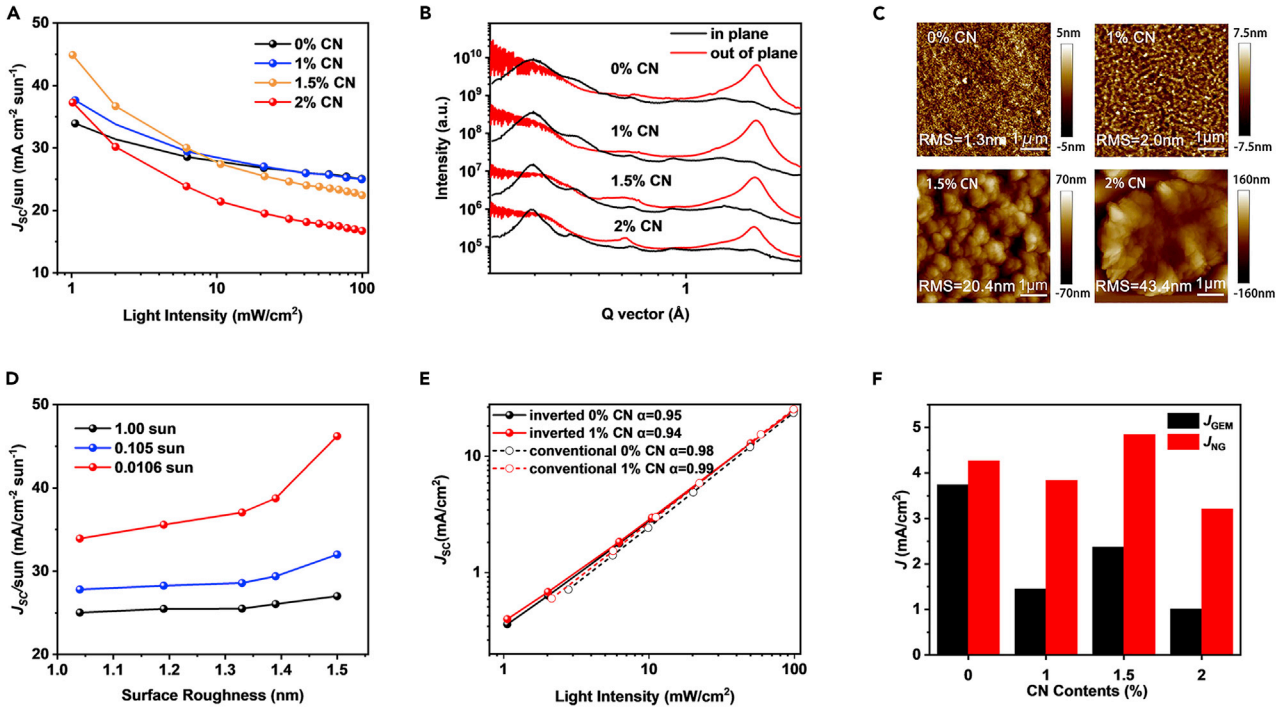

Figure 4. The effect of morphology on J_{SC} overestimation and overestimated J_{SC} on performance

(A) The J_{SC}/sun for PM6:Y6 devices with various CN contents.

(B and C) GIWAXS line profiles (B) and AFM height (C) of PM6:Y6 blend films with 0%, 1%, 1.5%, and 2% CN.

(D) The J_{SC}/sun for PM6:Y6 devices with different film surface roughness under different light intensity.

(E) Dependence of short-circuit current density on light intensity for inverted and conventional devices.

(F) The J_{GEM} and J_{NG} calculated by TDCF measurement for devices with various CN contents.

could be connected to device parameters such as recombination rate, carrier mobilities, and light scattering, these parameters are usually not light intensity dependent and do not lead to such significant J_{SC} overestimation.

The J_{SC} overestimation will inevitably bring errors in device analysis. It is apparent that the PCE slightly increases with decreasing the light intensity, as shown in Figure S24. Therefore, the PCE under low light intensities must be exceedingly overestimated due to the overestimation of J_{SC}. It also should be noticed that the fitted slopes (α) of J_{SC} and light intensity curves are commonly adopted to analyze the bimolecular recombination,[19] and the overestimation of J_{SC} will result in a wrong analysis. As shown in Figure 4E, the fitted slopes (α) are 0.95 and 0.94 for the inverted devices with 0% CN and 1% CN, respectively, representing that the device with 0% CN has lower bimolecular recombination. However, this result is contrary to the trend of their FFs. On the contrary, the fitted α for conventional devices with 0% CN and 1% CN are 0.98 and 0.99, respectively, which is consistent with FF trends (their *J-V* curves are shown in Figure S25). Furthermore, the time-delayed collection field (TDCF) measurement is applied to study the charge recombination for inverted devices.[46,47] The geminate recombination current (J_{GEM}) and non-geminate recombination (J_{NG}) can be calculated from the curves shown in Figure S26,[48] and the results are concluded in Table S5 and shown in Figure 4F. The J_{NG} of the device with 1% CN is smaller than that of the device with 0% CN, which is also contrary to the trend of the fitted α for the inverted device. These results sufficiently demonstrate that the J_{SC} overestimation under low light intensities will induce an erroneous

analysis for the charge recombination when using the relationship between J_{SC} and light intensity.

Conclusions

In this work, the equivalent circuit model is utilized to quantitatively investigate the electrical edge effect with light intensity and surface resistance of the active layer. The simulation shows that with 1 MΩ/sq surface sheet resistance, under low light, the edge effect will lead to significantly overestimated J_{SC} and PCE by over 70% and 22%, respectively. Such significant J_{SC} and PCE overestimation phenomenon applies for all types of solar cells, including OPVs, perovskite, and DSSC. The interface-doping-induced edge effect is experimentally confirmed by MoO_X-capped devices with varied photoactive layer systems, where J_{SC} and PCE could be overestimated by 51% and 15% under 0.01 sun, respectively. Besides, we analyzed the relationship among surface morphology of active layer and surface resistance and the consequent electrical edge effect, where J_{SC} overestimation increases significantly with surface roughness. Therefore, to reduce the electrical-edge-effect-induced J_{SC} overestimation error, we suggest taking the following measures: (1) apply mask during measurement, (2) larger device (>1 × 1 cm), (3) lower the surface roughness (<2 nm), and (4) conduct EQE measurement with light spot smaller than the device area. This work provided important new insights on the intrinsic mechanism of electric edge effect and its influence on device performance evaluation, especially under low light intensity, thereby promoting a healthier development of solar cell fields.

EXPERIMENTAL PROCEDURES

Resource availability

Lead contact

Further information and requests for resources and materials should be directed to and will be fulfilled by the lead contact, Wei Ma (msewma@xjtu.edu.cn).

Materials availability

All the materials were purchased from Solarmer Materials and eFlexPV without further purification.

Data and code availability

All data are present in the paper and supplemental information. Other data are available from the lead contact or corresponding author.

OPVs fabrication

The inverted devices were fabricated with a structure of glass/ITO/ZnO/PM6:Y6/MoO_X/Al. The patterned ITO substrate was continuously cleaned three times by sonication in water with detergent, deionized water, acetone, and isopropanol for 30 min of each step. Then, the substrate was dried with a nitrogen gun. After ultraviolet ozone treatment for 20 min, the ZnO precursor was spin coated on the ITO substrate at 4,500 rpm to form an electron transporting layer ZnO. Then, the substrate was baked at 200°C for 30 min. The active layer solution was prepared in chloroform (with 0% CN, 1% CN,1.5% CN and 2% CN) at a total concentration of 16 mg/mL with the D/A ratio of 1:1 by weight, accompanied by stirring on a hotplate at 50°C for at least 6 h. Then, a ~100 nm active layer was deposited by spin coating, followed by thermal annealing at 100°C for 10 min in the glovebox. Finally, a 10 nm MoO_3 and 100 nm Al were sequentially deposited as anode below the vacuum level of 1×10^{-4} Pa. The conventional devices were fabricated with a structure of ITO/PEDOT:PSS/PM6:Y6/PDINO/Al. A hole-transporting layer of PEDOT:PSS was deposited on

ITO by spin coating at 5,500 rpm for 30 s, followed by thermal annealing at 140°C for 10 min. The processing of active layer is same as the inverted devices. PDINO methanol solution (2.0 mg/mL) was then spin coated on the active layer at 3,300 rpm for 30 s to afford a buffer layer with a thickness of 10 nm. Finally, 100 nm Al was sequentially deposited as top electrode under vacuum (<1 × 10^{-4} Pa).

Measurements of OPVs

The *J-V* characteristics were performed in N_2-filled glovebox under AM 1.5G (100 mW/cm^2) by using a Keithley 2400 source meter unit and an AAA solar simulator (SS-F5-3A, Enli Technology) calibrated by a standard Si photovoltaic cell with a KG5 filter. The EQE was measured by a solar cell spectral response measurement system (QE-R3018, Enli Technology) with the calibrated light intensity by a standard single-crystal Si photovoltaic cell, and the neutral filter with different transmittances were used to adjust the light intensity. The UV-vis absorption spectra were measured on a Shimadzu UV-3600 Plus Spectrophotometer. PL spectra were performed on PTI Quanta Master 400 UV/VIS Spectrofluorometer at the excitation wavelength of 800 nm. The surface topography of the active layer was recorded by AFM operated in the tapping mode.

Time-delayed collection field (TDCF)

The TDCF experiment was carried out on OPV devices using the same strategy as these works.[49,50] It was conducted in an N_2 environment, inside a glovebox with O_2 ~ 0.1 ppm and H_2O <0.1 ppm. Pump excitation was achieved using an neodymium-doped yttrium aluminum garnet (ND-YAG)-pumped optical parametric oscillator (OPO) device (3 ns pulse width running at 100 Hz, Ekspla NT232) with a fluence of 100 nJ/cm^2. After the laser pulse, a device is given a time delay of 5 ns to allow for charge separation to happen before applying the collection field (sweep out voltage). The collection voltage was established via a custom-made amplification circuit, synched with the laser pulse, and a 250 MHz bandwidth function generator (Tektronix AFG 3251). To eliminate the effect of the resistor-capacitance (RC) time constant for a faster collection time before significant bimolecular recombination, we employ an over pulse strategy that uses an initial high voltage to charge the device electrodes more quickly. TDCF was conducted at two different laser wavelengths 600 and 810 nm, which were selectively chosen to match peaks from the UV-vis absorption for donor and acceptor molecules, respectively. The total generated charges were calculated from the photocurrent transients (light minus dark transients) that were measured using Teledyne LeCroy HDO 4104 with a 12-bit, 1 GHz bandwidth oscilloscope.

Photocurrent mapping

The photocurrent mappings of the solar cell were carried out by the photocurrent mapping system in dark. The photocurrent mapping system mainly consists of a displacement platform, a laser (model: CHT1230) and a Keithley 2400. The stepper was employed to control the position of device in the displacement platform. The longitudinal step is 0.02 mm, and the transverse step is 0.05 mm. The wavelength of laser is 650 nm, and the spot area is 0.001 mm^2. The current values of the device were recorded by the Keithley 2400.

Grazing incidence wide-angle X-ray scattering (GIWAXS) characterization

GIWAXS measurements were performed at beamline 7.3.3[43] at the Advanced Light Source. Samples were prepared on Si substrates using identical blend solutions as those used in devices. The 10 keV X-ray beam was incident at a grazing angle of 0.12°–0.16°, selected to maximize the scattering intensity from the samples. The scattered X-rays were detected using a Dectris Pilatus 2M photon counting detector.

Hole and electron mobility measurements

The mobilities were measured using hole-only device of glass/ITO/PEDOT:PSS/PM6:Y6/MoO_3/Al and electron-only device of glass/ITO/ZnO/PM6:Y6/PDINO/Al in space-charge-limited-current (SCLC) region. Hole mobility and electron mobility were obtained by fitting the current-density-voltage curves with:

$$J = 9\varepsilon_0\varepsilon_r\mu\left(V_{appl} - V_{bi} - V_s\right)^2 \Big/ 8L^3,$$

where J is current density, ε_0 is the permittivity of free space, ε_r is the relative permittivity of the material ($\varepsilon_r = 3$), μ is hole mobility or electron mobility, V_{appl} is the applied voltage, V_{bi} is the built-in voltage (0 V), V_s is the voltage drop from the substrate's series resistance ($V_s = IR$), and L is the film thickness.

SUPPLEMENTAL INFORMATION

Supplemental information can be found online at https://doi.org/10.1016/j.joule.2022.06.008.

ACKNOWLEDGMENTS

Thanks for the support from NSFC (21704082, 21875182, and 22109125), Key Scientific and Technological Innovation Team Project of Shaanxi Province (2020TD-002), China Postdoctoral Science Foundation (2017M623162), 111 Project 2.0 (BP2018008), and U.S. National Science Foundation DMR Electronic and Photonics Program under grant #1905790. X-ray data were acquired at beamlines 7.3.3 and 11.0.1.2 at the Advanced Light Source, which is supported by the Director, Office of Science, Office of Basic Energy Sciences of the U.S. Department of Energy under contract no. DE-AC02-05CH11231. The authors thank Chenhui Zhu at beamline 7.3.3 and Cheng Wang at beamline 11.0.1.2 for their assistance with data acquisition.

AUTHOR CONTRIBUTIONS

X.Z., C.Z., and W.M. conceived and designed the research. X.Z. designed the experiments and performed device fabrications. C.Z. and X.Z. performed the simulations. A.N.A. performed the TDCF test. H.W. performed the photocurrent mapping test. X.Z., C.Z., and W.M. drafted the manuscript. B.L. and K.Z. revised the manuscript. Z.M. and B.A.C. provided the academic instruction on this work.

DECLARATION OF INTERESTS

The authors declare no competing interests.

Received: January 21, 2022
Revised: March 22, 2022
Accepted: June 8, 2022
Published: July 6, 2022

REFERENCES

1. Bi, P., Zhang, S., Chen, Z., Xu, Y., Cui, Y., Zhang, T., Ren, J., Qin, J., Hong, L., Hao, X., and Hou, J. (2021). Reduced non-radiative charge recombination enables organic photovoltaic cell approaching 19% efficiency. Joule *5*, 2408–2419.

2. Hong, L., Yao, H., Cui, Y., Bi, P., Zhang, T., Cheng, Y., Zu, Y., Qin, J., Yu, R., Ge, Z., and Hou, J. (2021). 18.5% Efficiency organic solar cells with a hybrid planar/bulk heterojunction. Adv. Mater. *33*, e2103091.

3. Li, C., Zhou, J., Song, J., Xu, J., Zhang, H., Zhang, X., Guo, J., Zhu, L., Wei, D., Han, G., et al. (2021). Non-fullerene acceptors with branched side chains and improved molecular packing to exceed 18% efficiency in organic solar cells. Nat. Energy *6*, 605–613.

4. Liu, Q., Jiang, Y., Jin, K., Qin, J., Xu, J., Li, W., Xiong, J., Liu, J., Xiao, Z., Sun, K., et al. (2020). 18% Efficiency organic solar cells. Sci. Bull. *65*, 272–275.

5. Xu, Y., Cui, Y., Yao, H., Zhang, T., Zhang, J., Ma, L., Wang, J., Wei, Z., and Hou, J. (2021). A new conjugated polymer that enables the integration of photovoltaic and light-emitting functions in one device. Adv. Mater. *33*, e2101090.

6. Bai, F., Zhang, J., Zeng, A., Zhao, H., Duan, K., Yu, H., Cheng, K., Chai, G., Chen, Y., Liang, J., et al. (2021). A highly crystalline non-fullerene acceptor enabling efficient indoor organic

photovoltaics with high EQE and fill factor. Joule *5*, 1231–1245.

7. Ma, L.-K., Chen, Y., Chow, P.C.Y., Zhang, G., Huang, J., Ma, C., Zhang, J., Yin, H., Hong Cheung, A.M., Wong, K.S., et al. (2020). High-efficiency indoor organic photovoltaics with a band-aligned interlayer. Joule *4*, 1486–1500.

8. Zimmermann, E., Ehrenreich, P., Pfadler, T., Dorman, J.A., Weickert, J., and Schmidt-Mende, L. (2014). Erroneous efficiency reports harm organic solar cell research. Nat. Photonics *8*, 669–672.

9. Brabec, C.J., Distler, A., Du, X., Egelhaaf, H.J., Hauch, J., Heumueller, T., and Li, N. (2020). Material strategies to accelerate OPV technology toward a GW technology. Adv. Energy Mater. *10*, 2001864.

10. Zhang, Y., Ye, L., and Hou, J. (2017). Precise characterization of performance metrics of organic solar cells. Small Methods *1*, 1700159.

11. Cui, Y., Hong, L., and Hou, J. (2020). Organic photovoltaic cells for indoor applications: opportunities and challenges. ACS Appl. Mater. Interfaces *12*, 38815–38828.

12. Cravino, A., Schilinsky, P., and Brabec, C.J. (2007). Characterization of organic solar cells: the importance of device layout. Adv. Funct. Mater. *17*, 3906–3910.

13. Cui, Y., Hong, L., Zhang, T., Meng, H., Yan, H., Gao, F., and Hou, J. (2021). Accurate photovoltaic measurement of organic cells for indoor applications. Joule *5*, 1016–1023.

14. Lübke, D., Hartnagel, P., Angona, J., and Kirchartz, T. (2021). Comparing and quantifying indoor performance of organic solar cells. Adv. Energy Mater. *11*, 2101474.

15. Venkatesan, S., Lin, W.H., Teng, H., and Lee, Y.L. (2019). High-efficiency bifacial dye-sensitized solar cells for application under indoor light conditions. ACS Appl. Mater. Interfaces *11*, 42780–42789.

16. Pham, H.D., Jain, S.M., Li, M., Wang, Z.K., Manzhos, S., Feron, K., Pitchaimuthu, S., Liu, Z., Motta, N., Durrant, J.R., and Sonar, P. (2020). All-rounder low-cost dopant-free D-A-D hole-transporting materials for efficient indoor and outdoor performance of perovskite solar cells. Adv. Electron. Mater. *6*, 1900884.

17. Venkatesan, S., Lin, W.-H., Hsu, T.-H., Teng, H., and Lee, Y.-L. (2022). Indoor dye-sensitized solar cells with efficiencies surpassing 26% using polymeric counter electrodes. ACS Sustainable Chem. Eng. *10*, 2473–2483.

18. Park, S.Y., Li, Y., Kim, J., Lee, T.H., Walker, B., Woo, H.Y., and Kim, J.Y. (2018). Alkoxybenzothiadiazole-based fullerene and nonfullerene polymer solar cells with high shunt resistance for indoor photovoltaic applications. ACS Appl. Mater. Interfaces *10*, 3885–3894.

19. Qin, Y., Uddin, M.A., Chen, Y., Jang, B., Zhao, K., Zheng, Z., Yu, R., Shin, T.J., Woo, H.Y., and Hou, J. (2016). Highly efficient fullerene-free polymer solar cells fabricated with polythiophene derivative. Adv. Mater. *28*, 9416–9422.

20. Xu, X., Bi, Z., Ma, W., Wang, Z., Choy, W.C.H., Wu, W., Zhang, G., Li, Y., and Peng, Q. (2017). Highly efficient ternary-blend polymer solar cells enabled by a nonfullerene acceptor and two polymer donors with a broad composition tolerance. Adv. Mater. *29*, 1704271.

21. Yao, H., Chen, Y., Qin, Y., Yu, R., Cui, Y., Yang, B., Li, S., Zhang, K., and Hou, J. (2016). Design and synthesis of a low bandgap small molecule acceptor for efficient polymer solar cells. Adv. Mater. *28*, 8283–8287.

22. Riedel, I., Parisi, J., Dyakonov, V., Lutsen, L., Vanderzande, D., and Hummelen, J.C. (2004). Effect of temperature and illumination on the electrical characteristics of polymer–fullerene bulk-heterojunction solar cells. Adv. Funct. Mater. *14*, 38–44.

23. Jung, J.W., and Jo, W.H. (2015). Low-bandgap small molecules as non-fullerene electron acceptors composed of benzothiadiazole and diketopyrrolopyrrole for all organic solar cells. Chem. Mater. *27*, 6038–6043.

24. Sun, C., Qin, S., Wang, R., Chen, S., Pan, F., Qiu, B., Shang, Z., Meng, L., Zhang, C., Xiao, M., et al. (2020). High efficiency polymer solar cells with efficient hole transfer at zero highest occupied molecular orbital offset between methylated polymer donor and brominated acceptor. J. Am. Chem. Soc. *142*, 1465–1474.

25. Fan, B., Zhang, D., Li, M., Zhong, W., Zeng, Z., Ying, L., Huang, F., and Cao, Y. (2019). Achieving over 16% efficiency for single-junction organic solar cells. Sci. China Chem. *62*, 746–752.

26. Gevorgyan, S.A., Eggert Carlé, J., Søndergaard, R., Trofod Larsen-Olsen, T., Jørgensen, M., and Krebs, F.C. (2013). Accurate characterization of OPVs: device masking and different solar simulators. Sol. Energy Mater. Sol. Cells *110*, 24–35.

27. Tong, C., Ji, W., Li, D., Mei, A., Hu, Y., Rong, Y., and Han, H. (2019). Modeling the edge effect for measuring the performance of mesoscopic solar cells with shading masks. J. Mater. Chem. A *7*, 10942–10948.

28. Ito, S., Nazeeruddin, M.K., Liska, P., Comte, P., Charvet, R., Péchy, P., Jirousek, M., Kay, A., Zakeeruddin, S.M., and Grätzel, M. (2006). Photovoltaic characterization of dye-sensitized solar cells: effect of device masking on conversion efficiency. Prog. Photovolt.: Res. Appl. *14*, 589–601.

29. Servaites, J.D., Ratner, M.A., and Marks, T.J. (2009). Practical efficiency limits in organic photovoltaic cells: functional dependence of fill factor and external quantum efficiency. Appl. Phys. Lett. *95*, 163302.

30. Snaith, H.J. (2012). How should you measure your excitonic solar cells? Energy Environ. Sci. *5*, 6513.

31. Kiermasch, D., Gil-Escrig, L., Bolink, H.J., and Tvingstedt, K. (2019). Effects of masking on open-circuit voltage and fill factor in solar cells. Joule *3*, 16–26.

32. Lee, Y.-J., Adkison, B.L., Xu, L., Kramer, A.A., and Hsu, J.W.P. (2016). Comparison of conventional and inverted organic photovoltaic devices with controlled illumination area and extraction layers. Sol. Energy Mater. Sol. Cells *144*, 592–599.

33. Chen, Z., Wang, J., Jin, H., Yang, J., Bao, Q., Ma, Z., Tress, W., and Tang, Z. (2021). An underestimated photoactive area in organic solar cells based on a ZnO interlayer. J. Mater. Chem. C *9*, 11753–11760.

34. Tan, J.K., Png, R.Q., Zhao, C., and Ho, P.K.H. (2018). Ohmic transition at contacts key to maximizing fill factor and performance of organic solar cells. Nat. Commun. *9*, 3269.

35. Zhao, C., Tang, C.G., Seah, Z.L., Koh, Q.M., Chua, L.L., Png, R.Q., and Ho, P.K.H. (2021). Improving organic photovoltaic cells by forcing electrode work function well beyond onset of Ohmic transition. Nat. Commun. *12*, 2250.

36. Zhou, M., Chua, L.L., Png, R.Q., Yong, C.K., Sivaramakrishnan, S., Chia, P.J., Wee, A.T., Friend, R.H., and Ho, P.K. (2009). Role of δ-hole-doped interfaces at Ohmic contacts to organic semiconductors. Phys. Rev. Lett. *103*, 036601.

37. Kotadiya, N.B., Lu, H., Mondal, A., Ie, Y., Andrienko, D., Blom, P.W.M., and Wetzelaer, G.A.H. (2018). Universal strategy for Ohmic hole injection into organic semiconductors with high ionization energies. Nat. Mater. *17*, 329–334.

38. Tang, C.G., Syafiqah, M.N., Koh, Q.M., Zhao, C., Zaini, J., Seah, Q.J., Cass, M.J., Humphries, M.J., Grizzi, I., Burroughes, J.H., et al. (2019). Multivalent anions as universal latent electron donors. Nature *573*, 519–525.

39. Fang, J., Wang, Z., Zhang, J., Zhang, Y., Deng, D., Wang, Z., Lu, K., Ma, W., and Wei, Z. (2015). Understanding the impact of hierarchical nanostructure in ternary organic solar cells. Adv. Sci. (Weinh) *2*, 1500250.

40. Zhang, L., Lin, B., Ke, Z., Chen, J., Li, W., Zhang, M., and Ma, W. (2017). A universal approach to improve electron mobility without significant enlarging phase separation in IDT-based non-fullerene acceptor organic solar cells. Nano Energy *41*, 609–617.

41. Greiner, M.T., Chai, L., Helander, M.G., Tang, W.-M., and Lu, Z.-H. (2012). Transition metal oxide work functions: the influence of cation oxidation state and oxygen vacancies. Adv. Funct. Mater. *22*, 4557–4568.

42. Irfan, Ding, H., Gao, Y., Small, C., Kim, D.Y., Subbiah, J., and So, F. (2010). Energy level evolution of air and oxygen exposed molybdenum trioxide films. Appl. Phys. Lett. *96*, 243307.

43. Müller-Buschbaum, P. (2014). The active layer morphology of organic solar cells probed with grazing incidence scattering techniques. Adv. Mater. *26*, 7692–7709.

44. Hexemer, A., Bras, W., Glossinger, J., Schaible, E., Gann, E., Kirian, R., MacDowell, A., Church, M., Rude, B., and Padmore, H. (2010). A SAXS/WAXS/GISAXS beamline with multilayer monochromator. J. Phys.: Conf. Ser. *247*, 012007.

45. Zhou, X., Wu, H., Lin, B., Naveed, H.B., Xin, J., Bi, Z., Zhou, K., Ma, Y., Tang, Z., Zhao, C., et al. (2021). Different morphology dependence for efficient indoor organic photovoltaics: the role of the leakage current and recombination losses. ACS Appl. Mater. Interfaces *13*, 44604–44614.

46. Foertig, A., Kniepert, J., Gluecker, M., Brenner, T., Dyakonov, V., Neher, D., and Deibel, C. (2014). Nongeminate and geminate

recombination in PTB7:PCBM solar cells. Adv. Funct. Mater. *24*, 1306–1311.

47. Kniepert, J., Lange, I., van der Kaap, N.J., Koster, L.J.A., and Neher, D. (2014). A conclusive view on charge generation, recombination, and extraction in as-prepared and annealed P3HT:PCBM blends: combined experimental and simulation work. Adv. Energy Mater. *4*, 1301401.

48. Albrecht, S., Janietz, S., Schindler, W., Frisch, J., Kurpiers, J., Kniepert, J., Inal, S., Pingel, P., Fostiropoulos, K., Koch, N., and Neher, D. (2012). Fluorinated copolymer PCPDTBT with enhanced open-circuit voltage and reduced recombination for highly efficient polymer solar cells. J. Am. Chem. Soc. *134*, 14932–14944.

49. Dhakal, P., Ferron, T., Alotaibi, A., Murcia, V., Alqahtani, O., and Collins, B.A. (2021). Evidence for field-dependent charge separation caused by mixed phases in polymer-fullerene organic solar cells. J. Phys. Chem. Lett. *12*, 1847–1853.

50. Ferron, T., Waldrip, M., Pope, M., and Collins, B.A. (2019). Increased charge transfer state separationviareduced mixed phase interface in polymer solar cells. J. Mater. Chem. A *7*, 4536–4548.